

Refractory phosphorus in the HD 100546 protoplanetary disk

Mihkel Kama^{1,2*}, Oliver Shorttle³, Sandipan P. D. Borthakur², Luke Keyte^{1,4},
Jennifer B. Bergner⁵, Luca Fossati⁶, Colin P. Folsom², Heleri Ramler²

¹Department of Physics and Astronomy, University College London, Gower Street, London, WC1E 6BT, UK

²Tartu Observatory, University of Tartu, Observatooriumi 1, Tõravere, 61602, Estonia

³Institute of Astronomy, University of Cambridge, Madingley Road, Cambridge, CB3 0HA, UK

⁴Astronomy Unit, School of Physics and Astronomy, Queen Mary University of London, London E1 4NS, UK

⁵University of California, Berkeley, Department of Chemistry, Berkeley, CA 94720, USA

⁶Space Research Institute, Austrian Academy of Sciences, Schmiedlstrasse 6, 8042 Graz, Austria

Accepted XXX. Received YYY; in original form ZZZ

ABSTRACT

The phosphorus budget of planets is intertwined with their formation history and is thought to influence their habitability. The chemical reservoirs and volatile vs refractory budget of phosphorus in planet-forming environments have so far eluded empirical characterisation. We employ high-resolution spectra from HST/STIS in the ultraviolet and APEX in the sub-mm to constrain the phosphorus budget in the well-characterized HD 100546 star and protoplanetary disk system. We measure $\log (P/H)_{\star} = -7.50^{+0.23}_{-0.28}$ on the stellar surface, which traces the total inventory of P in accreting gas *and* dust from the inner disk. The inner disk gas, inside of the main dust trap, has $\log (P/H)_{\text{in}} \lesssim -8.70$, and the outer disk gas $\log (P/H)_{\text{out}} \lesssim -9.30$. Phosphorus in the disk is carried by a relatively refractory reservoir, consistent with minerals such as apatite or schreibersite, or with ammonium phosphate salts, in terms of sublimation temperature. We discuss the impact this might have on the two protoplanets around HD 100546. Our results contribute to our understanding of the chemical habitability of planetary systems and lay a foundation for future explorations, especially in the context of JWST and *Ariel* which can study phosphorus in exoplanet atmospheres.

Key words: astrochemistry – planets and satellites: formation – protoplanetary disks – stars: chemically peculiar – Herbig Ae/Be stars

1 INTRODUCTION

How phosphorus (P) arrives in planets, and in what abundance, is of particular importance across astrophysics, Earth, and planetary sciences. The phosphorus abundance in the envelopes of giant planets constitutes one of the clues to their formation history (Öberg & Wordsworth 2019). P also has an essential role in biology, in the information-carrying molecules of life (Westheimer 1987), and prebiotic chemistry (as a buffer and reagent; Patel et al. 2015). As the debate around the phosphine detection in Venus’s atmosphere has illustrated (e.g., Greaves et al. 2021; Villanueva et al. 2021; Lincowski et al. 2021), gas-phase phosphorus also has potential as a biosignature, albeit this interpretation is critically dependent on the magnitude and chemistry of abiotic exogenous and endogenous sources (Sousa-Silva et al. 2020; Bains et al. 2021). The phosphorus chemistry of planetary atmospheres and surfaces is therefore a key consideration in the search for life on exoplanets in the era of JWST, Ariel, and high-resolution ground-based spectroscopy.

Phosphorus exhibits a diverse behaviour in astrophysical and exoplanetary contexts: it undergoes a journey from its formation in stars, to the diffuse and dense interstellar medium, to planets that may take it from gas, to solid, and potentially back to gas again, whilst transitioning across a wide range of oxidation states (from -3 to +5; e.g., Jenkins 2009a; Pasek et al. 2007). This rich chemical behaviour means there is still much to be understood about the distribution and chemistry of phosphorus in planetary systems. Developing this understanding is ultimately a foundation to prospecting the universe for life — phosphorous is a key part of chemical habitability (Krijt et al. 2023).

Phosphorus begins its journey to planets in the interstellar medium, having been synthesised and delivered by dying massive stars. It is usually classed as a (semi-)refractory element, locked in solids at equilibrium temperatures ≤ 1229 K (Lodders 2003), but observations of the diffuse atomic interstellar medium indicate that all elemental P is accounted for by *atomic gas* in the most diffuse ISM regions (Jenkins 2009b, and references therein). The gas-phase phosphorus budget in the molecular interstellar medium is thought to be dominated by three species: PO, PN, and HCP

* E-mail: m.kama@ucl.ac.uk

(Mininni et al. 2018; Chantzos et al. 2020), with the latter being mainly seen around evolved stars. PO and PN are easily synthesized in the gas phase (Thorne et al. 1984; Millar et al. 1987). Progressive improvements to the phosphorus chemical network yield the same overall conclusion regarding the main gas-phase reservoirs (Adams et al. 1990; Millar 1991; MacKay & Charnley 2001; Aota & Aikawa 2012; Jiménez-Serra et al. 2018; Chantzos et al. 2020; Sil et al. 2021; Fernández-Ruz et al. 2023).

Since the first detection of PN in Orion KL and other high-mass star-forming regions (Ziurys 1987), PN, PO, and HCP have been found in various combinations in cold and warm star-forming cores (Fontani et al. 2016; Rivilla et al. 2016; Mininni et al. 2018; Wurmser & Bergner 2022), Galactic Centre clouds (Rivilla et al. 2018), and in outflows from protostars (Yamaguchi et al. 2011; Lefloch et al. 2016; Bergner et al. 2019) and evolved stars (Milam et al. 2008; De Beck et al. 2013). Additionally, HCP and PH₃ have been found in the outflowing envelope around the evolved star IRC+10216 (Agúndez et al. 2007, 2008, 2014).

The above observational studies find gas-phase PO, PN, and HCP abundances spanning three orders of magnitude: from as low as $X/H_2 = 10^{-10}$ to as high as the solar elemental P/H value 2.5×10^{-7} (Asplund et al. 2009). These values correspond to a range of depletions from strong, factor of 1000 depleted gas-phase elemental phosphorus, to undepleted within the uncertainties. The depletion of P from the gas phase is highly environment-dependent, with nearly all elemental phosphorus in the gas in the diffuse ISM (Jenkins 2009b). Observations of star-forming regions lend support to the importance of sputtering in keeping P-species in the gas phase, because diatomic P-bearing molecules are abundant in outflow-shocked material where solids are collisionally eroded (Mininni et al. 2018; Wurmser & Bergner 2022). In terms of thermal desorption, PO and PN have a desorption energy of $E_B = 1900$ K or 5770 K ($T_{\text{sub}} \approx 35$ K or 125 K; Rivilla et al. 2016; Piacentino & Öberg 2022), placing PO and PN in the domain of (hyper-)volatiles. Phosphine (PH₃) may be an important P-bearing ice species, but models suggest that in photon-dominated regions, such as the observable outer layers of protoplanetary disks, any PH₃ released into the gas is photodissociated; the released P then goes on to form PO and PN (Rivilla et al. 2020). There is a lack of gas-phase PN or PO towards hot core environments (e.g. Bernal et al. 2021; Fontani et al. 2024). Hot cores are the centrally irradiated, “hot” ($T_{\text{kin}} \gtrsim 100$ K) inner regions of protostellar cores (Wilson et al. 1979) where volatile ices sublimate (Garrod & Widicus Weaver 2013) and should be detectable in the gas. It is therefore unlikely that grain-phase P is mainly in a volatile ice such as PN, PO, or PH₃. Instead, these molecules are likely formed in the gas after shock sputtering of a semi-volatile grain carrier like apatite minerals (Bergner et al. 2022).

Thermodynamic models have shown that P condensation in a disk is highly sensitive to pressure, assumed gas-phase species, and the details of condensation (Sears 1978; Fegley & Lewis 1980). Equilibrium condensation models for early solar system conditions indicate that phosphorus first transfers from the gas into the mineral schreibersite (with a half mass condensation temperature $T_{50\%} \sim 1229$ K at solar composition; Lodders 2003), before transforming to phosphate minerals at lower temperatures ($T < 800$ K; Pasek 2019).

Whilst in the solar system we have a record of the P-bearing condensation products and their altered forms in the form of primitive CI chondrites containing schreibersite and apatite (e.g., Morlok et al. 2006), the poorly known initial conditions and chemical evolution of disks and planetesimals mean these only give us a partial insight into how phosphorus generally behaves in planet-forming

environments. Our new observations of phosphorus in a planet-forming disk and its accretion-dominated host star will fill this gap, and directly probe its gas-solid phase partitioning.

Stars earlier than type F5 ($M_\star \gtrsim 1.4 M_\odot$) do not have deep convective mixing in their envelope, rather being dominated by rotational mixing and diffusion (Turcotte 2002). This allows accretion from a protoplanetary disk to “contaminate” the observable photosphere (Jermyn & Kama 2018). The abundance of dust-forming elements has been shown to be low on the surface of Herbig Ae/Be stars that have strong dust traps (visible as bright dust rings) in their disks, the so-called “transitional disks” (Kama et al. 2015; Guzmán-Díaz et al. 2023). The presence of a strong dust trap removes refractory elements from the accretion stream, and this provides a diagnostic method to measure the refractory fraction of volatile and semi-volatile elements. We have previously used this method to determine the refractory fraction of sulfur ($89 \pm 8\%$ locked in refractory solids; Kama et al. 2019).

The depletion behaviour of phosphorus from the gas phase is not yet fully understood, so observations of P-carriers in physically well-characterised environments are needed to more accurately model its partitioning between specific gas- and solid-phase species before, and during, planet formation. In this paper, we apply the stellar accretion contamination method for the first empirical study of the major phosphorus carriers in a protoplanetary disk. This specifies the target selection criteria: an intermediate-mass young star with a transitional protoplanetary disk, both with well-characterised bulk parameters and as much information on chemical abundances as possible.

2 THE HD 100546 SYSTEM

The Herbig Ae/Be system HD 100546 consists of a well-characterised A0-type star ($2.4 M_\odot$) surrounded by a warm, flaring transitional disk. The large grains in the disk are trapped in an inner (22 to 40 au) and outer (150 to 230 au) dust ring. The outer dust gap and inner cavity each host a protoplanet candidate: HD 100546 b ($a_{\text{maj,b}} = 143$ au, $M_b = 3 M_{\text{Jup}}$) and c ($a_{\text{maj,b}} = 13$ au, $M_b = 8 M_{\text{Jup}}$; Pinilla et al. 2015; Pyerin et al. 2021). There is a significant literature on the source, we direct the reader to Benisty et al. (2010), Panić et al. (2010), Bruderer et al. (2012), Quanz et al. (2013), Walsh et al. (2014), Pinilla et al. (2015), Kama et al. (2016), Booth et al. (2021), Booth et al. (2024), and Keyte et al. (2023, 2024) as a starting point. The physical and chemical structure of the disk has been modelled in detail, reproducing observed rotational line emission from the main carbon-, oxygen-, and sulfur-carrying species. The temperature structure of the disk is such that the direct freeze-out of gas-phase hypervolatiles (e.g., CO) in the disk is negligible (Bruderer et al. 2012; Kama et al. 2016; Panić & Min 2017). The total volatile elemental C and O are not substantially depleted from the gas phase (Bruderer et al. 2012; Kama et al. 2016), while sulfur is depleted by a factor ~ 1000 with large radial variation (Keyte et al. 2023, 2024). The gas-phase abundances of C, O, and S vary radially and azimuthally (Keyte et al. 2023, 2024), implying the chemical composition of material available to accrete may differ for the two protoplanets.

3 OBSERVATIONS

To determine the budget of refractory and volatile phosphorus carriers in the planet-forming disk around HD 100546 (see Section 2),

Table 1. APEX sub-mm spectroscopic observations of HD 100546.

Date yyyy-mm-dd	ν_{LO} [GHz]	t_{exp} [hours]	PWV [mm] range
2018-07-30	234	2.4	0.9 ... 1.2
	234, 242	3.6	1.2 ... 1.6
2018-07-31	234, 242	4.8	1.0 ... 2.2
2018-08-03	242	2.8	1.6 ... 1.9
2018-11-06	242	2.5	1.2 ... 1.4
2018-08-08	242	3.9	2.6 ... 2.9
2018-11-07	234, 242	2.8	0.8 ... 1.6
2018-11-12	234	4.2	3.2 ... 3.9

Notes. The columns give the date (1), local oscillator frequency setting ν_{LO} (2), on-source exposure time (3), and precipitable water column (4). Grouped LO settings were observed in the same observing window on a given night.

we study emission in rotational transitions of P-bearing molecules (PO, PN, and HCP) in the disk gas and atomic absorption lines of P ionization states in the photosphere of the central star.

3.1 HST/STIS

To determine the stellar photospheric phosphorus abundance, we used archival spectra from the Space Telescope Imaging Spectrograph (STIS) on *Hubble* (HST). The high-resolution ($R \approx 114\,000$) data covered wavelengths from 1150 to 2887 Å and was downloaded from the StarCAT catalogue (see Data Availability). Two spectra of the star were available, taken on 2000-07-22 and 2000-11-04, with signal-to-noise $\text{SNR} \approx 10$ and ≈ 30 , respectively, at ≈ 1500 Å. We used the spectrum with the higher SNR.

The use of the HST/STIS spectrum to derive the stellar P/H ratio for HD 100546 is described in Section 4.1.

3.2 APEX

To study molecular emission lines of phosphorus-bearing species in the protoplanetary disk, observations of PO and PN rotational lines were carried out with the PI230 receiver and FFTS-4G backend on the APEX sub-millimetre telescope in 2018 (proposal E-0102.C-0927A). Two local oscillator settings were used: $\nu_{\text{LO}} = 234$ GHz for a set of PO and HCP lines and $\nu_{\text{LO}} = 242$ GHz for PN. A summary of the sub-millimetre observations is given in Table 1.

The APEX data underwent standard reduction procedures at ESO. After applying minor, low-order baseline corrections, we did not detect any of the targeted lines. The observing settings were chosen in such a way as to ensure that even upper limits would provide useful constraints on the gas-phase phosphorus budget, which we discuss in Section 4.2.

4 ANALYSIS

We investigate the phosphorus budget in the HD 100546 system by measuring its abundance relative to hydrogen on the stellar surface and in the disk gas. With the stellar surface measurement, we constrain the total amount of phosphorus passing through the last major dust trap and accreting onto the star; while, with the disk gas measurement, we constrain the fraction of elemental P locked in either dust grains or midplane ices.

Table 2. PO, PN, and HCP rotational transitions observed with APEX.

Mol.	Transition	ν_{ul} (GHz)	RMS (mK)	$T_{\text{A}} dv$ (mK $\frac{\text{km}}{\text{s}}$)
PN	$J = 5-4$	234.936	2.8	<13.2
HCP	$J = 6-5$	239.694	2.8	<26.4
PO	$J = \frac{11}{2} - \frac{9}{2}, F = 6-5, l = e$	239.949	2.8	<26.4
PO	$J = \frac{11}{2} - \frac{9}{2}, F = 5-4, l = e$	239.958	2.8	<26.4
PO	$J = \frac{11}{2} - \frac{9}{2}, F = 6-5, l = f$	240.141	2.5	<23.7
PO	$J = \frac{11}{2} - \frac{9}{2}, F = 5-4, l = f$	240.153	2.6	<24.6

Notes. Upper limits are given with 3σ confidence. The HCP line was not included in the modelling.

As a reference value, we adopt the solar abundance of phosphorus, $\log(\text{P}/\text{H})_{\odot} = -6.59 \pm 0.03$ (Asplund et al. 2009). An alternative would be the proto-solar value, but estimates differ significantly: Lodders (2003) estimated $\log(\text{P}/\text{H})_{\odot}^{\text{prot}} = -6.46 \pm 0.04$, while Asplund et al. (2021) suggest $\log(\text{P}/\text{H})_{\odot}^{\text{prot}} = -6.526$. We use the current solar abundance to place constraints on the unseen solid component. The abundances are conventionally expressed as the base-10 logarithm of the elemental number ratio $\log(\text{P}/\text{H})_{\star}$ for stellar photospheres, and as the absolute ratio for disk gas.

The disk around HD 100546 includes a bright inner dust ring from 22 to 40 au, and a faint outer ring from 150 to 230 au. We can assume a fraction δ_{L} of the inward-moving dust mass is trapped as large grains in the inner ring dust trap. This removes a corresponding fraction of the refractory component of each chemical element from each parcel of disk material. Thus, if 100 % of Fe in a parcel of disk material is contained in refractory dust, then $100 \times (1 - \delta_{\text{L}})$ % of all Fe would pass through the main dust trap and accrete onto the star, where it can be observed in the stellar photospheric composition as long as the mixing is slow and the accretion rate is high enough (Turcotte 2002; Jermyn & Kama 2018). This method allows to infer the fraction of each chemical element locked in solid particles. We apply it below to phosphorus.

The high disk accretion rate onto HD 100546, $\log(\dot{M}_{\text{acc}}) = -7.04^{+0.13}_{-0.15} \text{ M}_{\odot} \text{ yr}^{-1}$ (Fairlamb et al. 2015), leads the photospheric mixing fraction of freshly accreted material to be $f_{\text{acc}} = 98$ %, using a stellar mixing model that includes rotation, diffusion, and other processes (Jermyn & Kama 2022). The stellar photospheric composition is thus, to a high degree of accuracy, the elemental composition of the disk material *currently* accreting onto the star.

4.1 The accreted stellar phosphorus abundance

To measure the stellar photospheric P/H ratio, we adopted stellar parameters and known photospheric abundances for HD 100546 from Kama et al. (2016), who followed the spectral synthesis and fitting methodology of Folsom et al. (2012). The 2016 analysis did not include phosphorus due to a lack of suitable lines in the ESO FEROS spectrograph data. This is not unusual: because of a lack of suitable lines, the phosphorus abundance is rarely measured in intermediate-mass stars. Lines of P are however present in the HST/STIS spectrum we used. In our analysis of the STIS data, we employ the Zeeman spectral synthesis code (Landstreet 1988; Wade et al. 2001; Landstreet 2011; Folsom et al. 2012), ATLAS9 model atmospheres (Kurucz 1993; Castelli & Kurucz 2003) and a linelist from the Vienna Atomic Line Database (VALD; Piskunov et al. 1995; Ryabchikova et al. 1997; Kupka et al. 1999, 2000; Ryabchikova et al. 2015).

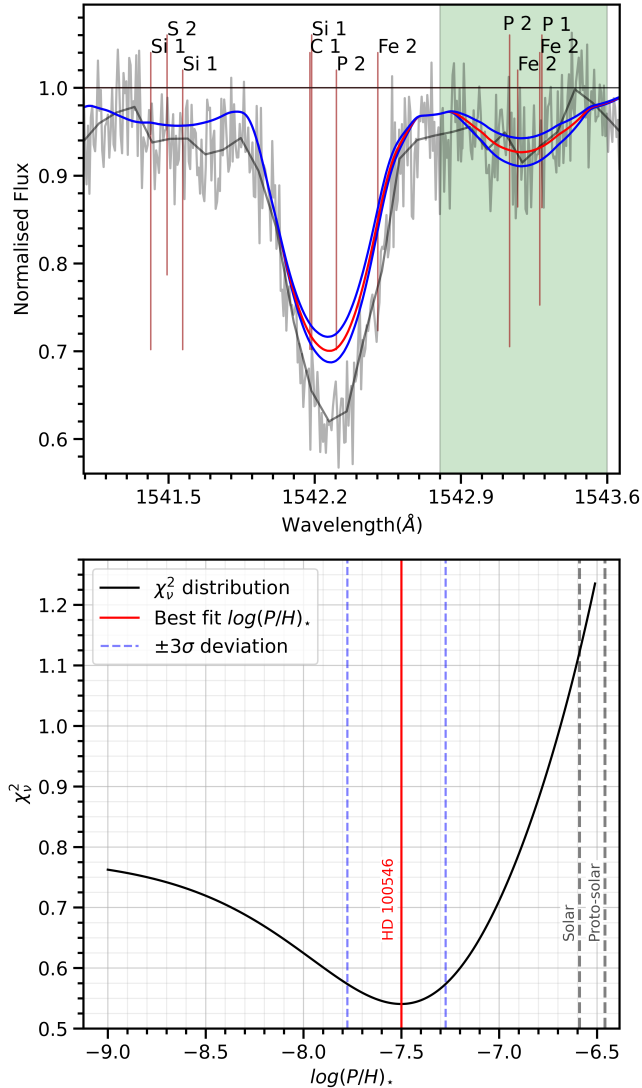


Figure 1. *Top panel:* The stellar spectrum of HD 100546 is in light grey, the binned spectrum is in dark grey, the red spectrum is the best-fit synthetic spectrum, and the blue spectra are for $\pm 3\sigma$ parameter deviations. The highlighted region is used for estimating $\log(\text{P}/\text{H})_*$ using the chi-square minimisation. *Bottom panel:* χ^2_v as a function of $\log(\text{P}/\text{H})_*$. The red vertical line indicates the minimum, while the blue lines are $\pm 3\sigma$ confidence intervals.

The lines in the STIS UV spectrum of HD 100546 are mostly blended due to crowding and rotational broadening ($v \sin i \approx 65 \text{ km s}^{-1}$). Our analysis of the weak phosphorus lines between 1301 and 1787 Å is further complicated by the low SNR and by inaccuracies in UV line parameters. Based on a visual inspection of the spectrum, we chose a small wavelength region from 1542.8 Å to 1543.5 Å, dominated by two P lines, as shown in the top panel of Figure 1. The stronger absorption feature at ≈ 1542.5 Å is a blend of a P II line with an equally strong carbon and slightly weaker silicon line. Our model of the strong P II feature likely suffers from errors in the C I and Si I line modelling. Adopting C/H and Si/H values from Kama et al. (2016), we find the stronger P II absorption feature is too deep to be explained by an excess of phosphorus abundance. This is because the excess phosphorus leads to a significant over-prediction of the weaker P I/P II line.

The accuracy of oscillator strengths is a concern in particular when analysing UV spectra. The weaker absorption feature is a blend of a singly ionised P II line at ≈ 1543.133 Å a neutral P I line at ≈ 1543.288 Å a Mn II line, and three Fe II lines. We tested the effect of the statistically weighted oscillator strength, $\log(g_l f_{lu})$, of the P and Fe lines, and found that P II dominates the weak feature. The $\log(g_l f_{lu})$ values of the P II and P I lines reported in the VALD database are -2.295 (Kurucz 2012) and -0.820 (Kurucz & Peytremann 1975), respectively.

To determine the stellar photospheric phosphorus abundance, $\log(\text{P}/\text{H})_*$, for HD 100546, we estimated the $\log(g_l f_{lu})$ value for the P II line at ≈ 1543.133 Å by a χ^2 -minimisation fitting of the HST/STIS spectrum of Vega with stellar parameters and photospheric abundances from Fitzpatrick (2010). This author determined $\log(\text{P}/\text{H})_*$ for Vega using an IUE spectrum with 78 lines of phosphorus. From our analysis of Vega, we obtained $\log(g_l f_{lu}) = -2.224$ for the P II line at ≈ 1543.133 Å. We adopted this for our analysis of HD 100546.

Using χ^2 minimisation on a continuum-normalised spectrum, we find the stellar photospheric phosphorus abundance in HD 100546 to be $\log(\text{P}/\text{H})_* = -7.50^{+0.23}_{-0.28}$ (3σ confidence; see Figure 1, right-hand panel). This result is validated with a fit on a second spectral region, which yields a $\log(\text{P}/\text{H})_*$ value within 1σ of the above result (see Appendix B).

4.1.1 Stellar parameters for the disk model

We use the absolute stellar spectrum constructed by Bruderer et al. (2012) using dereddened FUSE and IUE observations at UV wavelengths, and extended to longer wavelengths using the B9V template of Pickles (1998). The stellar luminosity is $36 L_\odot$ (Kama et al. 2016). The X-ray spectrum was characterized as a thermal spectrum with a temperature of 7×10^7 K from 1 to 100 keV, with a luminosity of $L_X = 7.94 \times 10^{28} \text{ erg s}^{-1}$.

4.2 Phosphorus in the protoplanetary disk gas

Next, we analyse the APEX data described Section 3.2 to constrain the total gas-phase elemental phosphorus abundance in the HD 100546 disk. We ran source-specific models using the 2D thermo-chemical code DALI (Bruderer et al. 2012; Bruderer 2013). Using an input stellar spectrum (Bruderer et al. 2012) and a 2D physical disk structure, the code iterates between continuum Monte Carlo radiative transfer and a chemistry solver to converge on the thermal and chemical structure of the disk, which allows to model outputs such as molecular lines. The disk structure we use for everything except the distribution of phosphorus species, is based on the HD 100546 disk model consecutively improved by Bruderer et al. (2012); Kama et al. (2016); Keyte et al. (2023, 2024). Below, we briefly restate some of the key features of the model. The adopted DALI model parameters are listed in Table A1.

The disk structure is parameterised, with a surface density that follows the standard form of a power law with an exponential taper:

$$\Sigma_{\text{gas}} = \Sigma_c \cdot \left(\frac{r}{R_c}\right)^{-\gamma} \exp\left[-\left(\frac{r}{R_c}\right)^{2-\gamma}\right] \quad (1)$$

where r is the radius, γ is the surface density exponent, and the reference surface density at R_c is Σ_c/e . The dust surface density is $\Sigma_{\text{gas}}/\Delta_{g/d}$, where $\Delta_{g/d}$ is the gas-to-dust mass ratio. The vertical distribution of gas follows a Gaussian with scale height:

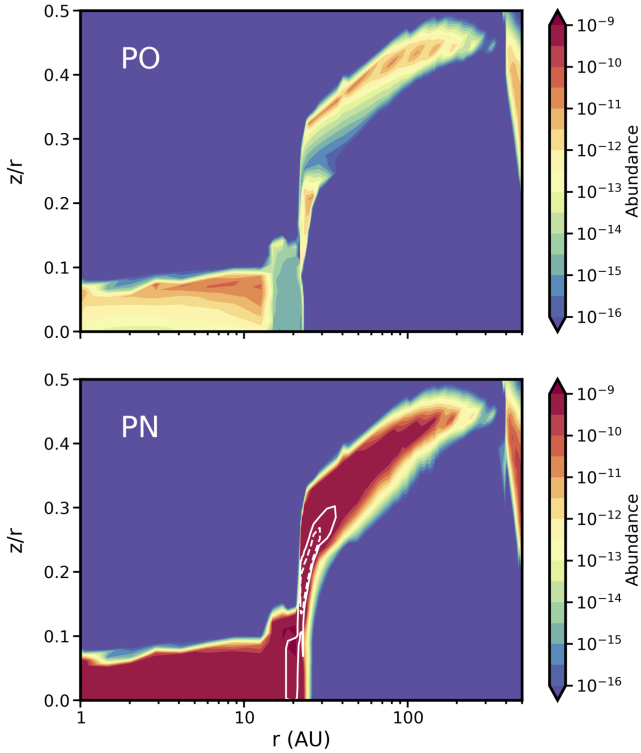


Figure 2. PO and PN abundance maps from our DALI model assuming a global volatile phosphorus abundance $P/H = 10^{-9}$. The white contours enclose 50 % and 75 % of total line flux for the PN 234.936 GHz transition.

$$h(r) = h_c \left(\frac{r}{R_c} \right)^\psi \quad (2)$$

where h_c is the scale height at R_c , and the power law index of the scale height, ψ , describes the flaring of the disk.

Σ_{gas} and Σ_{dust} extend from the dust sublimation radius ($R_{\text{sub}} = 0.25$ au) to the edge of the disk ($R_{\text{out}} = 500$ au), and can be varied independently inside the cavity radius R_{cav} with the multiplication factors δ_{gas} and δ_{dust} .

Dust settling is implemented by considering two different populations of grains: small grains (0.005-1 μm) and large grains (0.005-1 mm). The vertical density structure of the dust is such that large grains are settled towards the midplane, prescribed by the settling parameter, χ^1 :

$$\rho_{\text{dust, large}} = \frac{f \Sigma_{\text{dust}}}{\sqrt{2\pi} r \chi h} \exp \left[-\frac{1}{2} \left(\frac{\pi/2 - \theta}{\chi h} \right)^2 \right] \quad (3)$$

$$\rho_{\text{dust, small}} = \frac{(1-f) \Sigma_{\text{dust}}}{\sqrt{2\pi} r h} \exp \left[-\frac{1}{2} \left(\frac{\pi/2 - \theta}{h} \right)^2 \right] \quad (4)$$

where f is the mass fraction of large grains and θ is the opening angle from the midplane as viewed from the central star. Both grain populations follow a size distribution prescribed by a power law with index $q = -3.5$.

¹ Note that the dust settling parameter χ is distinct from the χ^2 statistic used elsewhere in the paper.

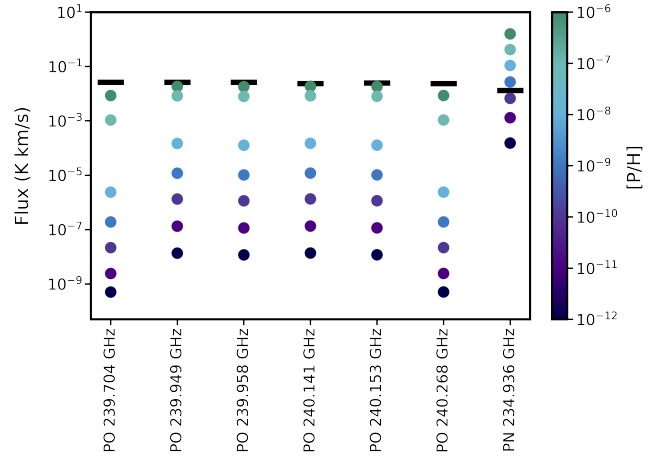


Figure 3. Volatile elemental P/H in the HD 100546 disk assuming a globally constant abundance. Disk-integrated 3σ line flux upper limits for the PO and PN transitions observed with APEX (black lines), and predicted line fluxes for a DALI model grid covering volatile elemental phosphorus abundances from $P/H = 10^{-12}$ to 10^{-6} (colored circles) are shown.

4.2.1 Chemical network

The chemical reaction network used in our model is based on a subset of UMIST 06 (Woodall et al. 2007). It consists of 145 species (including neutral and charged PAHs) and 1814 individual reactions. The DALI code includes H_2 formation on dust, freeze-out, thermal desorption, hydrogenation, gas-phase reactions, photodissociation and -ionization, X-ray induced processes, cosmic-ray induced reactions, PAH/small grain charge exchange/hydrogenation, and reactions with vibrationally excited H_2 . Non-thermal desorption is only included for a small number of species (CO , CO_2 , H_2O , CH_4 , NH_3). For grain surface chemistry, only hydrogenation of simple species is considered (C , CH , CH_2 , CH_3 , N , NH , NH_2 , O , OH). The details of these processes are described in Bruderer et al. (2012). For the present study, we have updated the network with 26 phosphorus-bearing species and 135 reactions from UMIST. Binding energies for all P-bearing species are set to $E_B = 5770$ K following the values determined for PO and PN by Piacentino & Öberg (2022), equivalent to a sublimation temperature of $T \approx 125$ K. The elemental abundances used in our model are listed in Table A2.

4.2.2 Molecular excitation and transition data

We adopted data for PO and PN rotational energy levels and transitions from the LAMDA database (Schöier et al. 2005; Toboła et al. 2007; Lique et al. 2018). Some necessary corrections to the energy level ordering were made by J.Bergner.

4.2.3 Gas-phase elemental P/H in the disk

To constrain the volatile elemental phosphorus abundance in the disk, we used a two-stage modelling approach:

Firstly, to get a rough estimate of the global depletion of gas-phase phosphorus, we modelled the disk-integrated PO and PN line flux upper limits using a constant volatile P/H ratio across the whole disk. Representative gas-phase PO and PN number abundance maps can be seen in Figure 2. The modelled line fluxes, with volatile elemental phosphorus values from $P/H = 10^{-12}$ to 10^{-6} (solar-like),

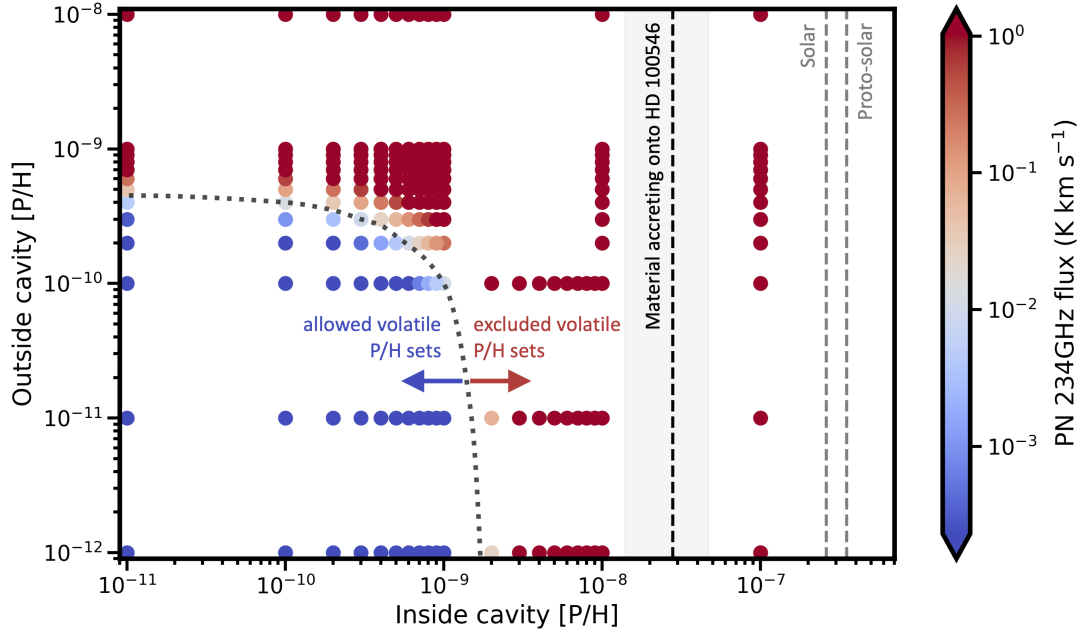


Figure 4. Coupled constraints on the gas-phase elemental P/H ratio inside (P/H_{in} , x-axis) and outside (P/H_{out} , y-axis) the 22 au dust cavity in the HD 100546 disk. Allowed abundance sets (shades of blue) meet the constraint from the PN line disk-integrated 3σ flux upper limit. The inner cavity P/H value is compared with the ratio as measured on the star for the accreting material, $(P/H)_{\star}$, and the solar (Asplund et al. 2009) and proto-solar (Lodders 2003) values.

are shown in Figure 3. The PO lines provided a weak constraint on the volatile phosphorus: $P/H \lesssim 10^{-6}$, which is an order of magnitude higher than the solar value. Our globally constant total elemental gas-phase P/H is based on the PN 6 – 5 line, from which we find $(P/H)_{\text{global}} \lesssim 5 \times 10^{-10}$.

Secondly – and this is our final, best-fit model – we modelled the data by dividing the disk into two radial zones with an independent gas-phase P/H ratio: one for material inside the inner edge of the main dust ring (i.e., inside the 22 au dust cavity; P/H_{in}), and another for the outer disk (P/H_{out}). This two-zone model was motivated by the abrupt change in temperature near the edge of the large dust cavity, with the temperature reaching ≈ 180 K at the inner edge of the dust ring (Keyte et al. 2023); and by the assumption that inward-drifting pebbles would stop in the dust ring and release their volatile ices. The results are shown in Figure 4 and show that a useful set of upper limits, described by a surface in the $(P/H)_{\text{in}}$, $(P/H)_{\text{out}}$ coordinate space, can be obtained. Looking at the extreme values for both axes, we independently constrain the gas-phase total P/H ratio inside the dust ring to be $P/H_{\text{in}} \lesssim 2 \times 10^{-9}$, while outside the dust ring we find $P/H_{\text{out}} \lesssim 5 \times 10^{-10}$.

Since the two protoplanet candidates are located inside (planet c) and outside (planet b) the main dust ring, the P/H_{in} and P/H_{out} limits can, respectively, be associated with gas currently being accreted by the protoplanets.

5 DISCUSSION

We have identified that, in the HD 100546 system, the total elemental gas-phase phosphorus abundance is depleted inside the main dust ring by a factor ≥ 129 and outside this zone by a factor ≥ 513 (obtained assuming a solar reference abundance and dividing that by the inner and outer disk upper limits from Section 4.2). We also find that the total (gas *plus* solid) elemental P is depleted in the dust-depleted disk material accreting onto the star by a factor ≈ 8

(obtained from dividing the solar reference by the $\log(P/H)_{\star}$ from Section 4.1). These results provide independent insights into the behaviour of P in the HD 100546 system, which we discuss below.

5.1 Phosphorus volatility in the HD 100546 disk

The factor of 8 depletion of phosphorus on the stellar surface, identified above (see Section 4.1), is consistent with the factor of ~ 10 overall depletion of refractory elements on the stellar surface (Kama et al. 2016).

In addition to a factor of ≈ 8 depletion of P, the accretion-dominated photosphere of the star HD 100546 is depleted in other refractory elements, also by approximately a factor of 10 (e.g., Mg, Ca, Si, Al; see Appendix A in Kama et al. 2016). This is despite the disk itself having an overall a gas-to-dust ratio of $\Delta_{\text{gd}} = 10$ –100 (e.g., Bruderer et al. 2012; Kama et al. 2016). Together, these observations imply that approximately 90 % of the inward-moving dust mass from the outer disk does not currently reach the star.

The most significant finding from the two-zone disk model is that the total gas-phase phosphorus abundance in the inner cavity is $P/H_{\text{in}} < 2 \times 10^{-9}$, which is at least 16 times less than the abundance on the stellar photosphere. We identify the stellar P/H_{\star} value with the total gas *plus* solid abundance of phosphorus in the inner cavity. In other words, P/H_{\star} represents any and all carriers of phosphorus that are carried past the main dust ring and through the inner cavity. Given the large difference between P/H_{\star} and P/H_{in} , the two-zone disk model strongly suggests that most of the phosphorus passing through the dust cavity is contained in small dust grains, hidden from the gas-phase chemistry probed by our ALMA observations.

The values of P/H_{star} and P/H_{in} are thus consistent with a scenario where most of the inward-moving dust mass has gotten trapped, most likely in the prominent dust ring at 22 to 40 au, leaving the inner cavity deprived of large dust grains (pebbles) and the stellar surface deprived of dust-forming elements. Only small dust grains,

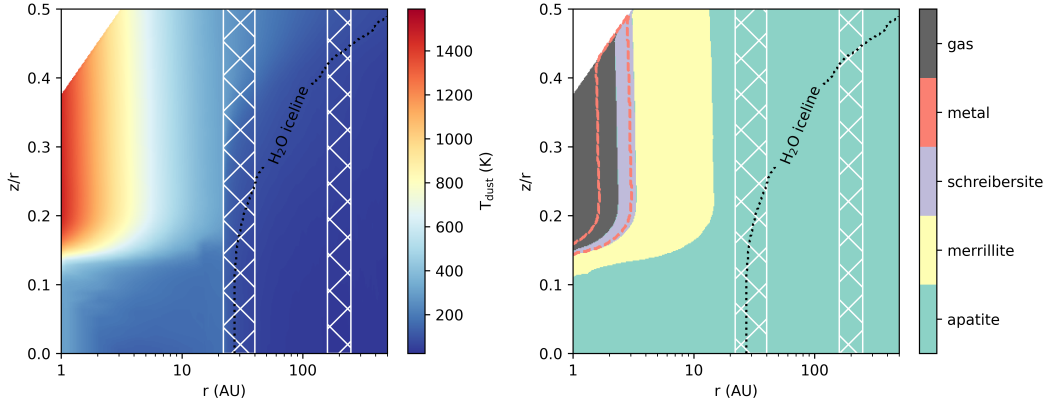


Figure 5. The dominant phosphorous reservoirs throughout the HD 100546 disk. *Left-hand panel:* a map of the calculated disk temperature structure, which dictates phosphorous mineral stability. Normalised height above midplane is given by z/r , with height above midplane, z (au), divided by the radial distance, r (au). Hatched regions indicate the two dust rings identified in this system and the dotted black line marks the water iceline (parameterised simply as the 121 K isotherm after Lodders 2003). *Right-hand panel:* a map of the dominant phosphorous reservoirs in the disk assuming equilibrium at the dust temperature. The minerals apatite, merrillite, and schreibersite progressively replace each other as the main phosphorous reservoir as temperature is increased, up to the point where temperatures are high enough that all major phosphorous-bearing mineral phases have sublimated and most phosphorous is in the gas phase. Phosphorous dissolved in Fe metal is never a dominant reservoir, but its presence is mapped by the dashed contour. Mineral stabilities were taken from Pasek (2019).

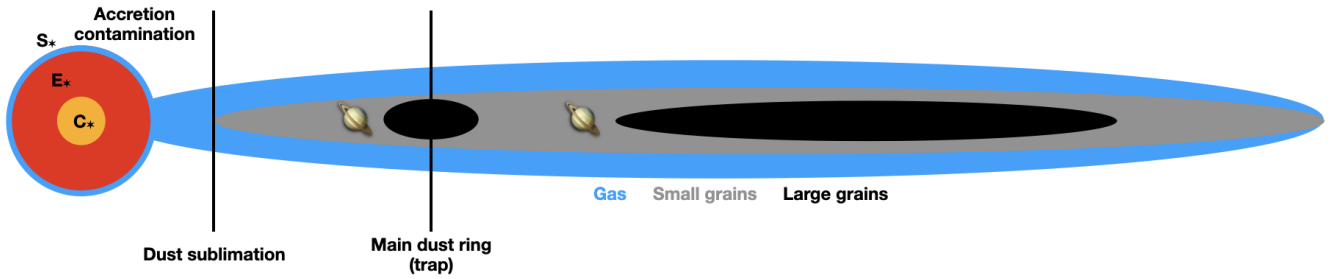


Figure 6. Sketch of the HD 100546 system with the star, protoplanetary disk, and two claimed protoplanets.

which are coupled to the gas but generally constitute a small fraction of the total dust mass, can traverse the inner cavity. In the HD 100546 disk model from Keyte et al. (2024), grains ≤ 1 mm in size constitute 5 % of the dust mass, which given the various uncertainties involved appears consistent with ≈ 10 % of refractories reaching the stellar surface. This general finding on refractories being depleted on the star due to dust trapping is in line with our previous work in Kama et al. (2016, 2019). The stellar and inner disk P/H values furthermore lead to the conclusion that the dominant phosphorus reservoir in the HD 100546 disk is sufficiently refractory to remain solid at the inner edge of the main dust belt, where the temperature reaches nearly 200 K.

We are here using “refractory” more broadly compared to its cosmochemical meaning, and use it to refer to anything less volatile than water ice. This distinction is made on the basis that the stellar oxygen abundance is normal, i.e. undepleted, in HD 100546 and other Herbig Ae/Be stars with dust-poor accretion. This constant O/H value regardless of whether the disk is transitional or full, is taken as evidence that H_2O ice, which is the dominant carrier of elemental O in disks, generally sublimates in the main dust trap in such transitional disks and freely accretes onto the star (Kama et al. 2019). Ice sublimation is in general more likely at the inner edge of dust traps, as temperatures rise due to increased illumination (Broome et al. 2023; Chen et al. 2024). In the case of HD 100546, the

lack of oxygen depletion is consistent with the matching locations of the water iceline and inner dust ring (Keyte et al. 2023, 2024, see also Figure 5).

We note that while the volatility trend of elemental depletions on the surface of accreting Herbig Ae/Be stars is consistent from the most volatile elements (C), through the intermediates (Na, S, Zn), to the most refractory ones (e.g., Fe, Ti), oxygen does not follow this trend (Kama et al. 2015, 2019). Instead, in material accreting onto Herbig Ae/Be stars oxygen has a refractory fraction of 0 ± 2 % (Kama et al. 2015). This may be due to with disk or stellar evolution processes, or systematics in the oxygen abundance measurements and is being investigated in a separate study. While this raises doubts as to the overall reliability of the oxygen abundance, we argue that the effect is likely mainly relevant for masking the minor refractory component of O. If H_2O ice, the expected major O carrier, was being trapped in the last major dust trap, the star would be receiving strongly oxygen-depleted material, which would then show a depletion signature of comparable magnitude to Fe or Ti.

This finding of elemental P being locked almost exclusively in dust is consistent with the temperature at the location of the dust trap, which predicts that – at equilibrium, which is a limiting assumption – most phosphorous at this location would be in refractory mineral form as apatite (Figure 5). We only include the equilibrium mineral composition as a secondary argument, to suggest that our findings are not

inconsistent with the P reservoirs expected in case the composition had time to equilibrate in the dust trap. Apatite or large phosphorus oxides (e.g. P_4O_{10}) with similar volatility were also inferred to be likely grain-phase carriers of phosphorus in the protostellar stage (Bergner et al. 2022).

5.2 The main phosphorus reservoir

The conclusion from above that most, or all, elemental P is locked in refractory solids. This solid P is most likely trapped in pebbles in the 22–40 au dust ring, similar to even more refractory elements such as iron, titanium, or aluminium. The accreted oxygen abundance on the HD 100546 stellar photosphere is consistent with almost no depletion, indicating almost all oxygen passes freely through the dust trap. If we assume the elemental O budget is dominated by H_2O , we can conclude the main reservoir of elemental phosphorus in the HD 100546 disk is more refractory than H_2O ice, so that it can remain trapped while H_2O ice sublimates. The temperature of the dust trap is ≈ 70 K (outer edge) to ≈ 180 K (inner edge), sufficient to sublimate water (Kama et al. 2016; Keyte et al. 2023).

Our empirical finding that almost all phosphorus is locked in solids that are more refractory than water ice is consistent with predictions from thermochemical equilibrium. As seen in Figure 5, we find that the preferred equilibrium reservoir is a mineral phase in much of the disk, and specifically in the inner dust ring. Equilibrium condensation sequence calculations place P in the refractory minerals schreibersite, apatite, or merrillite (Fegley & Lewis 1980; Lodders 2003; Pirim et al. 2014; Pasek 2019). We note that it is unclear whether thermochemical equilibrium is an appropriate assumption for the material in the HD 100546 dust ring.

Among meteorites, the main P reservoir in hydrous carbonaceous chondrites and ordinary chondrites is phosphates, such as apatite ($\geq 90\%$ of total elemental phosphorus), or schreibersite ($\leq 10\%$; Pasek & Lauretta 2008, and references therein). However, the *Rosetta* mission to comet 67P/Churyumov-Gerasimenko found no evidence for apatite and only weak consistency with schreibersite for the main P carrier in the cometary dust grains (Gardner et al. 2020). In samples from asteroid Ryugu, the main phosphorus-bearing phases were found to be apatite, schreibersite, and a new phase: hydrated ammonium-magnesium phosphorus (HAMP) grains (Pilorget et al. 2024). A similar list of P-carriers has been found in samples from asteroid Bennu (Lauretta et al. 2024).

Ammonium salts, such as the ammonium phosphate found recently on Ryugu (see above), have become a contender for carrying a significant fraction of nitrogen, sulfur, or other elements such as halogens in a semi-refractory reservoir, sublimating at a few hundred kelvins, based on solar system evidence (Poch et al. 2020; Altwegg et al. 2020, 2022). While we cannot rule out ammonium phosphate, $(\text{NH}_4)_3\text{PO}_4$, as the main carrier of phosphorus in the HD 100546 disk, it we also have no evidence for a significant total mass of diverse ammonium salts being withheld in the dust trap. This is because the accreted photospheric N/H ratio of HD 100546, $\log(\text{N}/\text{H})_\star = -3.82 \pm 0.30$ (Kama et al. 2016), is marginally super-solar, assuming $\log(\text{N}/\text{H})_\odot = -4.17 \pm 0.05$ (Asplund et al. 2009). Thus, we have no evidence for nitrogen depletion in the accretion stream.

On the other hand, the small fraction of elemental N needed to lock away only P atoms in ammonium phosphate would be too small to cause a measurable N depletion on the star ($3 \times \text{P}/\text{N} \approx 1\%$ for solar abundances) so we cannot rule it out. However, the lack of evidence of trapping of more abundant salt species in the dust trap then demands a very specific explanation. If ammonium phosphate

were an important P reservoir, a mechanism strongly favouring its formation over NH_4^+ salts with a more abundant anion (such as sulfate) would be required to explain the lack of measurable elemental N depletion in the HD 100546 stellar photosphere.

Our available evidence therefore favours a mineral reservoir, such as apatite or schreibersite, to account for most of the phosphorus. Ammonium phosphate is also a candidate, but it may not have a dominant role as we do not see a depletion of N that would indicate the presence of large amounts of diverse ammonium salts as a “volatile vault” in the dust belt where P is getting trapped.

5.3 The phosphorus budget of the protoplanets

As described in Section 2, the disk around HD 100546 is known to host at least two giant protoplanet candidates: HD 100546 b ($a_{\text{maj,b}} = 143$ au, $M_b = 3 M_{\text{Jup}}$) and c ($a_{\text{maj,b}} = 13$ au, $M_b = 8 M_{\text{Jup}}$; Pinilla et al. 2015; Pyerin et al. 2021). We illustrate the scenario for HD 100546 in Figure 6. Protoplanet b orbits in a wide dust gap radially outwards from the main dust trap (ring), while c orbits inwards of the trap (Walsh et al. 2014; Pinilla et al. 2015).

Our measurements above show that elemental P in the inner few tens of au of this disk can be accounted for entirely by a refractory reservoir: the depletion of phosphorus from the gas follows that of Fe, Mg, Si, and other refractories (see also Kama et al. 2015). In an imaginary parcel of homogeneously mixed disk material, almost all P would be contained in dust grains. Most of the dust mass is in large dust grains (pebbles) and thus settled on the midplane, where such large grains will drift into dust traps such as the main dust ring. A smaller fraction of total elemental P will be in small grains, which are kinematically coupled to the gas and not as sensitive to trapping in local gas pressure maxima.

The above implies the current availability of phosphorus may be very different for the protoplanets b and c. A giant planet may accrete material into its gas envelope either across the disk midplane, or through the surface via meridional flows (Teague et al. 2019; Szulágyi et al. 2022). As both planets have opened dust gaps, any currently ongoing midplane accretion would be dust-poor as large grains would not be able to accrete. Furthermore, we can hypothesise the inner planet (c) might be accreting particularly low-metallicity material as any solids would need to have first passed through *two* radial dust traps, with the inner trap apparently being the stronger of the two. If this is the case, planet c may end up with a lower metallicity, and a lower total elemental P/H ratio in its envelope compared to the outer planet, b.

If meridional flows dominate the currently ongoing accretion onto either of the planets, that planet (or both) would have a low envelope metallicity, with a correspondingly low elemental P/H ratio.

6 CONCLUSIONS

(i) We find a phosphorus abundance $\log(P/H)_\star = -7.50^{+0.23}_{-0.28}$ in the stellar photosphere. This is significantly below the solar value, $\log(P/H)_\odot = -6.59 \pm 0.03$. The slowly-mixing radiative envelope of the star and the high disk accretion rate imply the $(P/H)_\star$ value characterises the total P/H in the inner disk, where the accretion originates, and not the bulk of the star.

(ii) We find the total gas-phase elemental phosphorus abundance in the inner disk, inside the main dust ring, to be $(P/H)_{\text{in}} \lesssim 2 \times 10^{-9}$. We constrain the value outside the dust ring to be $(P/H)_{\text{out}} \lesssim 5 \times$

10^{-10} . These two values characterise P/H in the gas currently being accreted by protoplanet candidates c and b, respectively.

(iii) Phosphorus in the HD 100546 disk is strongly depleted from the gas into a refractory (dusty) reservoir. This is based on the above conclusions that phosphorus is strongly depleted from the disk gas everywhere, and depleted – but less severely – in the material (gas+dust) in the accretion stream. The main carrier of P in the inner cavity is predicted to be small dust grains that are not trapped in the dust ring at 22 to 40 au.

(iv) Apatite and schreibersite are favoured over volatile ices or ammonium salts as the dominant phosphorus reservoir in the grains, both on sublimation temperature grounds and on the grounds that we see the volatiles N, C, and O behaving differently from P in the inner disk.

(v) Our empirical finding that elemental phosphorus in the HD 100546 disk is carried entirely, or almost entirely, by dust suggests that the P/H ratio in giant planet envelopes traces their refractory element accretion history as well or even better than sulfur.

ACKNOWLEDGEMENTS

The authors thank Anish Amarsi for useful comments that helped to improve the manuscript. SB, CF, LF, and MK gratefully acknowledge funding from the European Union’s Horizon Europe research and innovation programme under grant agreement No. 101079231 (EXOHOST), and from UK Research and Innovation (UKRI) under the UK government’s Horizon Europe funding guarantee (grant number 10051045). LK acknowledges funding via a Science and Technology Facilities Council (STFC) studentship and by UKRI guaranteed funding for a Horizon Europe ERC consolidator grant (EP/Y024710/1).

DATA AVAILABILITY

The sub-millimetre spectroscopic observations of rotational lines of PO, PN, and HCP can be accessed on the APEX data archive², under the proposal code 0102.C-0927(A). The *Hubble* Space Telescope spectra are available through the StarCAT database³. Our disk model is available on request from the authors.

REFERENCES

Adams N. G., McIntosh B. J., Smith D., 1990, *A&A*, **232**, 443
 Agúndez M., Cernicharo J., Guélin M., 2007, *ApJ*, **662**, L91
 Agúndez M., Cernicharo J., Pardo J. R., Guélin M., Phillips T. G., 2008, *A&A*, **485**, L33
 Agúndez M., Cernicharo J., Decin L., Encrenaz P., Teyssier D., 2014, *ApJ*, **790**, L27
 Altwegg K., et al., 2020, *Nature Astronomy*, **4**, 533
 Altwegg K., et al., 2022, *MNRAS*, **516**, 3900
 Aota T., Aikawa Y., 2012, *ApJ*, **761**, 74
 Asplund M., Grevesse N., Sauval A. J., Scott P., 2009, *ARA&A*, **47**, 481
 Asplund M., Amarsi A. M., Grevesse N., 2021, *A&A*, **653**, A141
 Bains W., et al., 2021, *Astrobiology*, **21**, 1277
 Benisty M., Tatulli E., Ménard F., Swain M. R., 2010, *A&A*, **511**, A75
 Bergner J. B., Öberg K. I., Walker S., Guzmán V. V., Rice T. S., Bergin E. A., 2019, *ApJ*, **884**, L36

Bergner J. B., Burkhardt A. M., Öberg K. I., Rice T. S., Bergin E. A., 2022, *ApJ*, **927**, 7
 Bernal J. J., Koelemay L. A., Ziurys L. M., 2021, *ApJ*, **906**, 55
 Booth A. S., Walsh C., Terwisscha van Scheltinga J., van Dishoeck E. F., Ilee J. D., Hogerheijde M. R., Kama M., Nomura H., 2021, *Nature Astronomy*, **5**, 684
 Booth A. S., et al., 2024, *AJ*, **167**, 164
 Broome M., Kama M., Booth R., Shorttle O., 2023, *Monthly Notices of the Royal Astronomical Society*, **522**, 3378
 Bruderer S., 2013, *A&A*, **559**, A46
 Bruderer S., van Dishoeck E. F., Doty S. D., Herczeg G. J., 2012, *A&A*, **541**, A91
 Castelli F., Kurucz R. L., 2003, in Piskunov N., Weiss W. W., Gray D. F., eds, Vol. 210, *Modelling of Stellar Atmospheres*. p. A20 ([arXiv:astro-ph/0405087](https://arxiv.org/abs/10.48550/arXiv.astro-ph/0405087)), doi:10.48550/arXiv.astro-ph/0405087
 Chantzos J., Rivilla V. M., Vasyunin A., Redaelli E., Bizzocchi L., Fontani F., Caselli P., 2020, *Astronomy & Astrophysics*, **633**, A54
 Chen K., Kama M., Pinilla P., Keyte L., 2024, *MNRAS*, **527**, 2049
 De Beck E., Kamiński T., Patel N. A., Young K. H., Gottlieb C. A., Menten K. M., Decin L., 2013, *A&A*, **558**, A132
 Fairlamb J. R., Oudmaijer R. D., Mendigutía I., Ilee J. D., van den Ancker M. E., 2015, *MNRAS*, **453**, 976
 Fegley B. J., Lewis J. S., 1980, *Icarus*, **41**, 439
 Fernández-Ruz M., Jiménez-Serra I., Aguirre J., 2023, *ApJ*, **956**, 47
 Fitzpatrick E. L., 2010, *The Astrophysical Journal*, **725**, 2401
 Folsom C. P., Bagnulo S., Wade G. A., Alecian E., Landstreet J. D., Marsden S. C., Waite I. A., 2012, *MNRAS*, **422**, 2072
 Fontani F., Rivilla V. M., Caselli P., Vasyunin A., Palau A., 2016, *ApJ*, **822**, L30
 Fontani F., et al., 2024, *A&A*, **682**, A74
 Gardner E., et al., 2020, *MNRAS*, **499**, 1870
 Garrod R. T., Widicus Weaver S. L., 2013, *Chemical Reviews*, **113**, 8939
 Greaves J. S., et al., 2021, *Nature Astronomy*, **5**, 655
 Guzmán-Díaz J., Montesinos B., Mendigutía I., Kama M., Meeus G., Vioque M., Oudmaijer R. D., Villaver E., 2023, *A&A*, **671**, A140
 Jenkins E. B., 2009b, *ApJ*, **700**, 1299
 Jenkins E. B., 2009a, *The Astrophysical Journal*, **700**, 1299
 Jermyn A. S., Kama M., 2018, *MNRAS*, **476**, 4418
 Jermyn A. S., Kama M., 2022, *Research Notes of the American Astronomical Society*, **6**, 131
 Jiménez-Serra I., Viti S., Quénard D., Holdship J., 2018, *ApJ*, **862**, 128
 Kama M., Folsom C. P., Pinilla P., 2015, *A&A*, **582**, L10
 Kama M., et al., 2016, *A&A*, **592**, A83
 Kama M., Shorttle O., Jermyn A. S., Folsom C. P., Furuya K., Bergin E. A., Walsh C., Keller L., 2019, *ApJ*, **885**, 114
 Keyte L., et al., 2023, *Nature Astronomy*, **7**, 684
 Keyte L., Kama M., Chuang K.-J., Cleaves L. I., Drozdovskaya M. N., Furuya K., Rawlings J., Shorttle O., 2024, *MNRAS*, **528**, 388
 Krijt S., Kama M., McClure M., Teske J., Bergin E. A., Shorttle O., Walsh K. J., Raymond S. N., 2023, in Inutsuka S., Aikawa Y., Muto T., Tomida K., Tamura M., eds, *Astronomical Society of the Pacific Conference Series* Vol. 534, *Astronomical Society of the Pacific Conference Series*. p. 1031
 Kupka F., Piskunov N., Ryabchikova T. A., Stempels H. C., Weiss W. W., 1999, *A&AS*, **138**, 119
 Kupka F. G., Ryabchikova T. A., Piskunov N. E., Stempels H. C., Weiss W. W., 2000, *Baltic Astronomy*, **9**, 590
 Kurucz R., 1993, *ATLAS9 Stellar Atmosphere Programs and 2 km/s grid*. Kurucz CD-ROM No. 13. Cambridge, 13
 Kurucz R. L., 2012, Robert L. Kurucz on-line database of observed and predicted atomic transitions
 Kurucz R. L., Peytremann E., 1975, *SAO Special Report*, **362**, 1
 Landstreet J. D., 1988, *ApJ*, **326**, 967
 Landstreet J. D., 2011, *A&A*, **528**, A132
 Lauretta D. S., et al., 2024, *Meteoritics and Planetary Science*, **59**, 2453
 Lefloch B., et al., 2016, *MNRAS*, **462**, 3937
 Lincowski A. P., et al., 2021, *The Astrophysical Journal Letters*, **908**, L44

² <https://www.apex-telescope.org/ns/>

³ https://archive.stsci.edu/prepds/starcat/StarCAT_portal.html

Lique F., Jiménez-Serra I., Viti S., Marinakis S., 2018, *Physical Chemistry Chemical Physics (Incorporating Faraday Transactions)*, **20**, 5407

Lodders K., 2003, *ApJ*, **591**, 1220

MacKay D. D. S., Charnley S. B., 2001, *MNRAS*, **325**, 545

Milam S. N., Halfen D. T., Tenenbaum E. D., Apponi A. J., Woolf N. J., Ziurys L. M., 2008, *ApJ*, **684**, 618

Millar T. J., 1991, *A&A*, **242**, 241

Millar T. J., Bennett A., Herbst E., 1987, *MNRAS*, **229**, 41P

Mininni C., Fontani F., Rivilla V. M., Beltrán M. T., Caselli P., Vasyunin A., 2018, *MNRAS*, **476**, L39

Morlok A., Bischoff A., Stephan T., Floss C., Zinner E., Jessberger E. K., 2006, *Geochimica Cosmochimica Acta*, **70**, 5371

Öberg K. I., Wordsworth R., 2019, *AJ*, **158**, 194

Panić O., Min M., 2017, *MNRAS*, **467**, 1175

Panić O., van Dishoeck E. F., Hogerheijde M. R., Bellocche A., Güsten R., Boland W., Baryshev A., 2010, *A&A*, **519**, A110

Pasek M. A., 2019, *Icarus*, **317**, 59

Pasek M. A., Lauretta D., 2008, *Origins of Life and Evolution of the Biosphere*, **38**, 5

Pasek M. A., Dworkin J. P., Lauretta D. S., 2007, *Geochimica et Cosmochimica Acta*, **71**, 1721

Patel B. H., Percivalle C., Ritson D. J., Duffy C. D., Sutherland J. D., 2015, *Nature chemistry*, **7**, 301

Piacentino E. L., Öberg K. I., 2022, *ApJ*, **939**, 93

Pickles A. J., 1998, *PASP*, **110**, 863

Pilorget C., et al., 2024, *Nature Astronomy*, **8**, 1529

Pinilla P., Birnstiel T., Walsh C., 2015, *A&A*, **580**, A105

Pirim C., Pasek M. A., Sokolov D. A., Sidorov A. N., Gann R. D., Orlando T. M., 2014, *Geochimica Cosmochimica Acta*, **140**, 259

Piskunov N. E., Kupka F., Ryabchikova T. A., Weiss W. W., Jeffery C. S., 1995, *A&AS*, **112**, 525

Poch O., et al., 2020, *Science*, **367**, aaw7462

Pyerin M. A., Delage T. N., Kurtovic N. T., Gárate M., Henning T., Pinilla P., 2021, *A&A*, **656**, A150

Quanz S. P., Amara A., Meyer M. R., Kenworthy M. A., Kasper M., Girard J. H., 2013, *ApJ*, **766**, L1

Rivilla V. M., Fontani F., Beltrán M. T., Vasyunin A., Caselli P., Martín-Pintado J., Cesaroni R., 2016, *ApJ*, **826**, 161

Rivilla V. M., et al., 2018, *MNRAS*, **475**, L30

Rivilla V. M., et al., 2020, *MNRAS*, **492**, 1180

Ryabchikova T. A., Piskunov N. E., Kupka F., Weiss W. W., 1997, *Baltic Astronomy*, **6**, 244

Ryabchikova T., Piskunov N., Kurucz R. L., Stempels H. C., Heiter U., Pakhomov Y., Barklem P. S., 2015, *Phys. Scr.*, **90**, 054005

Schöier F. L., van der Tak F. F. S., van Dishoeck E. F., Black J. H., 2005, *A&A*, **432**, 369

Sears D. W., 1978, *Earth and Planetary Science Letters*, **41**, 128

Sil M., et al., 2021, *AJ*, **162**, 119

Sousa-Silva C., Seager S., Ranjan S., Petkowski J. J., Zhan Z., Hu R., Bains W., 2020, *Astrobiology*, **20**, 235

Szulágyi J., Binkert F., Surville C., 2022, *ApJ*, **924**, 1

Teague R., Bae J., Bergin E. A., 2019, *Nature*, **574**, 378

Thorne L. R., Anicich V. G., Prasad S. S., Huntress W. T. J., 1984, *ApJ*, **280**, 139

Tobola R., Kłos J., Lique F., Chafasiński G., Alexander M. H., 2007, *A&A*, **468**, 1123

Turcotte S., 2002, *ApJ*, **573**, L129

Villanueva G., et al., 2021, *Nature Astronomy*, **5**, 631

Wade G. A., Bagnulo S., Kochukhov O., Landstreet J. D., Piskunov N., Stift, M. J., 2001, *A&A*, **374**, 265

Walsh C., et al., 2014, *ApJ*, **791**, L6

Westheimer F. H., 1987, *Science*, **235**, 1173

Wilson T. L., Downes D., Bieging J., 1979, *A&A*, **71**, 275

Woodall J., Agúndez M., Markwick-Kemper A. J., Millar T. J., 2007, *A&A*, **466**, 1197

Wurmser S., Bergner J. B., 2022, *ApJ*, **934**, 153

Yamaguchi T., et al., 2011, *PASJ*, **63**, L37

Ziurys L. M., 1987, *ApJ*, **321**, L81

Table A1. DALI disk model parameters for HD 100546 (Keyte et al. 2023). See also Bruderer et al. (2012) and Kama et al. (2016).

Parameter	Description	Fiducial
R_{sub}	Sublimation radius	0.25 au
R_{gap}	Inner disk size	1.0 au
R_{cav}	Cavity radius	22 au
R_{out}	Disk outer radius	1000 au
R_c	Critical radius for surface density	50 au
δ_{gas}	Gas depletion factor inside cavity	10^{-5}
δ_{dust}	Dust depletion factor inside cavity	10^{-4}
γ	Surface density power law index	1.0
χ	Dust settling parameter	0.2
f	Large-to-small dust mixing	0.95
Σ_c	Σ_{gas} at R_c	87.25 g cm^{-2}
h_c	Scale height at R_c	0.10
ψ	Power law index of scale height	0.25
$\Delta_{\text{g/d}}$	Gas-to-dust mass ratio	100
L_*	Stellar luminosity	$36 L_{\odot}$
L_X	Stellar X-ray luminosity	$7.94 \times 10^{28} \text{ erg s}^{-1}$
T_X	X-ray plasma temperature	$7.0 \times 10^7 \text{ K}$
ζ_{cr}	Cosmic ray ionization rate	$3.0 \times 10^{-17} \text{ s}^{-1}$
M_{gas}	Disk gas mass	$9.89 \times 10^{-2} M_{\odot}$
M_{dust}	Disk dust mass	$1.06 \times 10^{-3} M_{\odot}$
t_{chem}	Chemical timescale	5 Myr

Table A2. Chemical element number abundances, relative to H nuclei, in the DALI model of the disk around HD 100546.

Species	n_i/n_{H}
<i>Fixed</i>	
H	1.0
He	9.0×10^{-2}
C	1.5×10^{-5}
N	6.2×10^{-5}
O	3.0×10^{-5}
S	1.0×10^{-8}
Mg	5.0×10^{-7}
Si	5.0×10^{-7}
Fe	5.0×10^{-7}

APPENDIX A: DISK MODEL PARAMETERS

In Table A1, we list the DALI model parameters adopted for the HD 100546 disk model. The elemental abundances assumed for elements other than P are listed in Table A2.

APPENDIX B: (P/H) $_{\star}$ FROM A SECOND SPECTRAL REGION

We also estimated the P abundance from the P II line between 1535.4 and 1536.4 Å. The P II line is blended with one S II and one Mn II line. No prior abundance measurement for Mn was available from Folsom et al. (2012), so we measured it from the following spectral regions: 1857.52–1859.13 Å, 1863.57–1865.29 Å, 1865.29–1870.33 Å, 1910.00–1912.00 Å, 1942.90–1945.95 Å, and 1916.70–1922.00 Å. We find $(\text{Mn}/\text{H})_{\star} = -7.56 \pm 0.35$. We applied this value to estimate $(\text{P}/\text{H})_{\star}$ from the spectral region highlighted in Figure B. By comparing with the Vega spectrum, we estimated the statistically weighted oscillator strength value for the P II line at

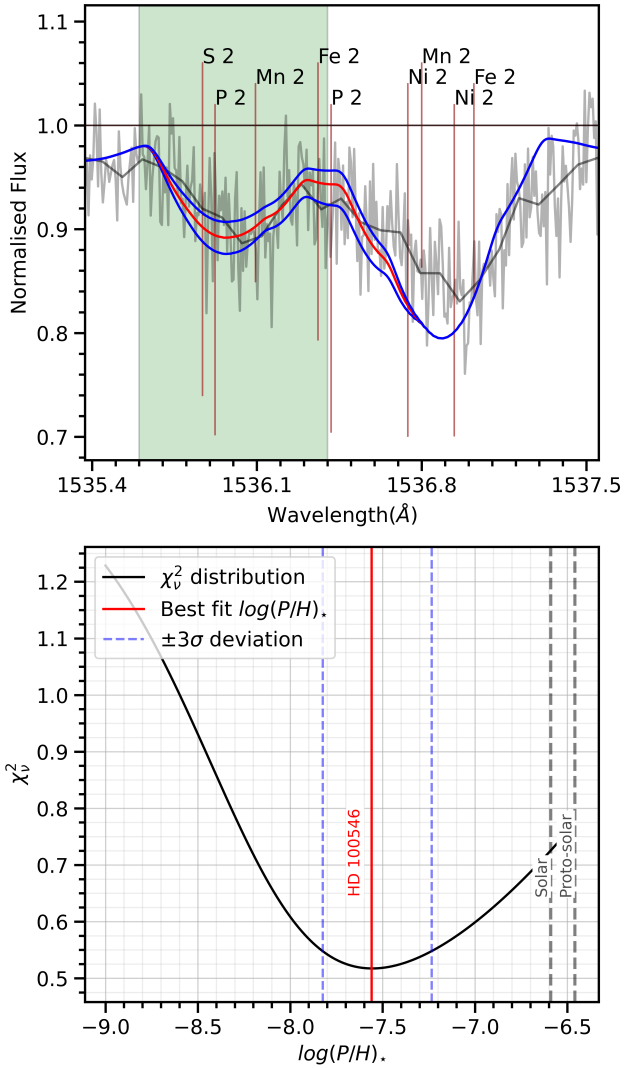


Figure B1. Determining $(P/H)_*$ for HD 100546 in a second spectral region. **Top panel:** The spectrum of HD 100546 at native (light grey) and binned resolution (dark grey). Overlays show the best-fit synthetic spectrum (red) and its range for $\pm 3\sigma$ parameter deviations (blue). The highlighted green region is used for estimating $\log(P/H)_*$ with chi-square minimisation. **Bottom panel:** χ^2 as a function of $\log(P/H)_*$. The red vertical line indicates the minimum (best fit), while the blue dashed lines are $\pm 3\sigma$ confidence intervals.

1535.9225 Å to be $\log(g_l f_{lu}) = -1.470$. The value for the P II line reported in VALD is $\log(g_l f_{lu}) = -1.765$. There is another P II line at 1536.4157 Å, which is not considered while fitting the spectra because the line is blended with two relatively strong Ni II lines which likely have incorrect $\log(g_l f_{lu})$ values, based on a comparison with the Vega spectrum. We could not estimate the $\log(g_l f_{lu})$ values for the other P II line and the two Ni II lines. Using the χ^2 minimisation technique described in Section 4.1, we estimated the P abundance from this spectral region to be $(P/H)_* = -7.56^{+0.32}_{-0.26}$ (3σ confidence; see Figure B, bottom panel). The best-fit value here is within 1σ of the main result presented in Section 4.1.

Aside from noise in the spectrum, two other sources of uncertainty affect our P abundance measurements - uncertainty in our $\log(g_l f_{lu})$ values and the uncertainty in our continuum placement.

For weak lines, the $\log(g_l f_{lu})$ of a spectral line is directly proportional to the inferred abundance of that element. Since our correction of $\log(g_l f_{lu})$ values for the P lines are based on the spectrum of Vega, we can use the P abundance uncertainty in Vega from Fitzpatrick (2010) to get the uncertainty in our $\log(g_l f_{lu})$. This gives an uncertainty of 0.05 dex in $\log(g_l f_{lu})$. The $\log(g_l f_{lu})$ value can also be affected by the S/N of the Vega spectrum. This uncertainty is ~ 0.06 dex. Assuming both uncertainties are uncorrelated, the combined uncertainty of the $\log(g_l f_{lu})$ value is ~ 0.08 dex. Thus, the uncertainty in our P abundance estimates of HD 100546 from $\log(g_l f_{lu})$ is 0.08 dex (1σ).

For the spectral regions discussed here and in Section 4.1, we shifted the continuum vertically to check its effect on the measured $(P/H)_*$. We found that a local continuum multiplier in excess of a factor of 1.005 makes the local spectral region inconsistent with the wider spectrum in terms of the low-order behaviour of the normalised spectrum. A continuum multiplier 1.005 in either direction for both spectral regions used to estimate $(P/H)_*$ changes the phosphorus abundance by $\approx \pm 0.11$ dex. This is smaller than the formal 3σ uncertainties we report for our results.

We did not consider here the uncertainty due to other stellar parameters and abundances since quantifying that is more complicated and was not considered as a source of uncertainty in Folsom et al. (2012). Although there might be additional sources of systematic uncertainties, such as incorrect $\log(g_l f_{lu})$ values of neighbouring blended lines, our comparison with the Vega spectrum suggests that such factors cannot offset the P depletion implied by our measurement.

This paper has been typeset from a \LaTeX file prepared by the author.